Investigation of fatigue crack initiation and growth in cast MAR-M247 subjected to low cycle fatigue at room temperature

Abstract:

MC carbide particles (with B1 lattice structure and constituent metallic element, M, being Hafnium/Tantalum) were observed to crack extensively in a cast polycrystalline nickel-base superalloy, MAR-M247, when subjected to low-cycle fatigue loading at room temperature. High resolution secondary electron images taken on the surface of a double edge notch test specimen revealed that approximately half the carbide particles had cracked in the highly-strained notch section of the specimen, and that the average surface area of cracked particles was approximately three times that of the uncracked particles. From the analysis of secondary electron images of cracked carbide particles, it was determined that the cracks within a large number of particles (with aspect ratio less than 3), aligned nearly perpendicular to the loading direction, where as in high aspect ratio particles (with aspect ratio greater than 3), the cracks aligned with the major axis of the particle, independent of the loading direction. Electron back scattered diffraction (EBSD) data coupled with energy dispersive spectroscopy (EDS) analysis showed that the cracked carbide particles were rich in Hafnium and Tantalum and a large portion of the cracked particles were located at grain boundaries. Additionally, forward-scattered imaging showed a high density of slip bands impinging on most of the particles that cracked. The life limiting crack growth in MAR-M247 was observed to be crystallographic in nature, as the crack grew along slip bands as measured by high-resolution EBSD (HREBSD), even after spanning many grains. Furthermore, crystal plasticity finite element (CPFE) simulations carried out on virtual microstructures, statistically representative of the MAR-M247 material examined, predicted that there was a significant variation in the stress state of carbide particles. These simulations showed that the microstructure of grains surrounding the carbide particles has an influence on the stress state of the particles. Additionally, the simulations revealed that the particles that reside on the surface are subject to higher stresses compared to those that reside within the bulk of the specimen.

1. Introduction

Cast MAR-M247 is a polycrystalline nickel-base superalloy well known for its high temperature strength, ductility, fatigue and creep resistance (Nathal et al. 1982). Grain boundary strengthening and enhancement of ductility at high temperatures is achieved in MAR-M247 through the formation of discrete MC particles (with B1 lattice structure and constituent metallic element, M, being Hafnium/Tantalum) and $M_{23}C_6$ carbide particles (with FCC lattice structure and constituent metallic element, M, being Chromium) during solidification (Chen et al. 1998) and thermal aging processes (Janowski 1985), respectively. The mechanical properties of MAR-M247 are greatly dependent on the size, morphology, volume fraction, and distribution of the carbide particles within the matrix of the material (Gell and Leveran 1968; Kotval et al. 1972; Kaufman 1984).

Several studies have aimed at characterizing the microstructure and identifying the mechanisms of crack initiation in polycrystalline MAR-M247 (Kotval et al. 1972; Wawro 1982; Kaufman 1984; Boismier and Sehitoglu 1990; Bor et al. 1999; Szczotok et al. 2006; Szczotok and Rodak 2012; Šmíd et al. 2014; Šmíd et al. 2016). While the Chromium rich $M_{23}C_6$ particles present

at the grain boundaries help resist grain boundary sliding and increase ductility at high temperature, brittle cracks initiated and contributed in providing a preferred path for crack propagation at the elongated Hafnium and Tantalum rich MC type carbide particles (Kotval et al. 1972; Wawro 1982). Although the aforementioned studies provide valuable microscopic observations of the role played by the morphology of MC carbides in promoting crack incubation and growth in polycrystalline MAR-M247, a study specifically addressing how the micromechanical deformation in the neighboring grains contributes to brittle fracture of carbides is still lacking. In the current work, microscopy data (secondary electron and forward-scattered electron imaging) combined with electron backscatter diffraction (EBSD) analysis was used to characterize the statistics of crack incubation sites, and micromechanics of deformation in the vicinity of cracked particles. High-resolution EBSD (HREBSD) analysis was used to map the dislocation density around the crack tip of a large crack, and determine the slip systems along which the crack was growing. Further, fatigue experiments and microscopy analysis need to be complemented with computational analysis to develop insights regarding the driving forces that promote crack incubation in the particles.

Over the past three decades, efforts were directed towards developing life prediction models (Sehitoglu and Boismier 1990; Brindley et al. 2015) for MAR-M247 subject to thermo-mechanical loading. These models do not take into consideration the microstructure attributes and the stress and strain heterogeneities within the microstructure, and hence they do not provide any insights regarding the influence of neighboring microstructure on particle failure. Various studies have used finite element analysis to model an inclusion (or particle) surrounded by matrix in order to study the i) combined effect of aspect ratio of the particle and orientation of grain surrounding the particle on the stress state of the particle (Bozek et al. 2008), ii) change in driving force for nucleation in a near-surface inclusion with the growth in oxide layer on the surface of a martensitic steel (Przybyla et al. 2010), iii) effect of neighboring orientation on the variation of plastic strain around an inclusion located close to a bi-crystal interface in a nickel-superalloy (Shenoy et al. 2005), and iv) influence of particle shape and the interface condition between the particle and the matrix in a carburized and shot-peened martensitic steel (Zhang et al. 2009). The aforementioned studies provide valuable insights for inclusion based fatigue crack nucleation and growth in various materials, but they are limited to single and bi-crystal models and hence cannot account for complexity and variability in the stress state of particles arising from the heterogeneity of the surrounding polycrystalline neighborhood. In the current work, virtual microstructures representative of polycrystalline MAR-M247 are used in a crystal plasticity finite element (CPFE) framework to quantify the variability in the stress state of the carbide particles, and to gain insights regarding various factors contributing to the variability in stress state of particles in the microstructure of MAR-M247.

The remainder of the paper is organized as follows. Section 2 discusses the test specimen geometry and microstructural characterization of MAR-M247 along with the specimen preparation procedure. Section 3 discusses the experimental setup for fatigue tests and digital image correlation for strain measurements. Section 4 includes results and discussions based on i) the observations from microscopy scans and ii) insights learned from CPFE simulations regarding various factors contributing to the significant variability in stress state within the carbide particles. Conclusions are provided in Section 5.

2. Fatigue test specimen and microstructure characterization of MAR-M247

The test specimens of MAR-M247 were sectioned longitudinally from a casting, as shown in Fig. 1a. Using electro discharge machining, a double edge notch is introduced at the mid-plane of the specimen (as shown in Fig. 1b and c) in such a way that the thickness at the center of the notch is equal to the thickness of a previously proposed thin, high-temperature component which is used in converting thermal energy into electrical energy on a deep-space mission spacecraft (Bowman et al. 2004; Schreiber and Thieme 2008). The microstructure of the component was produced to obtain optimal high temperature creep and fatigue properties (Wood et al. 2005), which is critical for thin section components.
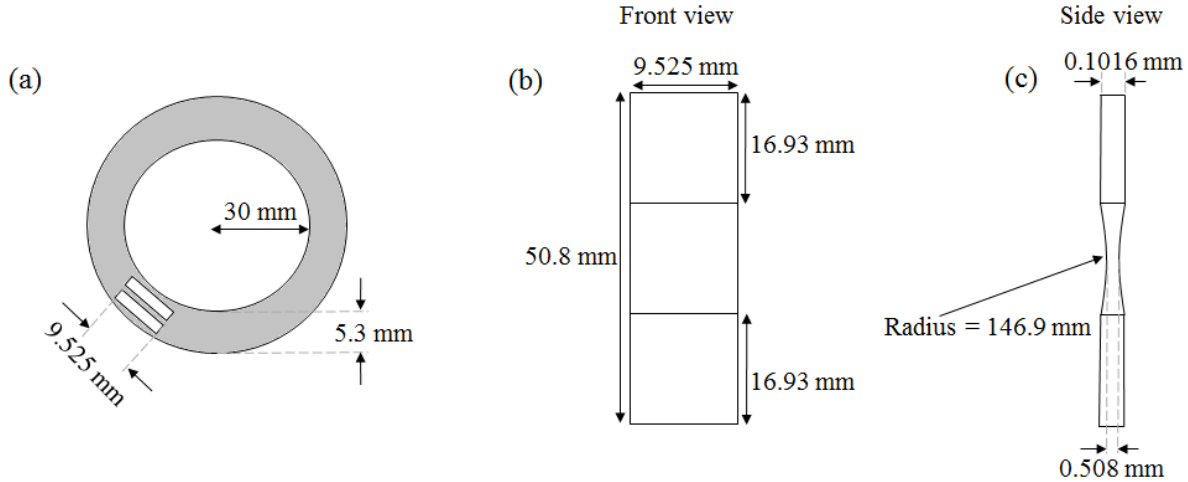

Fig. 1. a) Top view of the casting. Samples were sectioned from the hollow cylinder casting, as shown by the slots in the cylinder. Also shown is b) front and c) side views of the test specimen with the double edge notch.

The notch area of a double edge notched test specimen was polished in progression of 30-15-6-3-0.5 μm diamond polishing solution followed by 0.05 μm colloidal silica solution to obtain an EBSD quality surface. Subsequently, EBSD scans were obtained over the entire notch width. The EBSD data was used to quantitatively characterize the microstructure of MAR-M247. Grain size, orientation and misorientation distributions obtained from processing the EBSD data are shown in Fig 2. The average grain size was approximately 110 μm, with the size of the largest grain being 390 μm. Further, it was observed that the material had random texture.
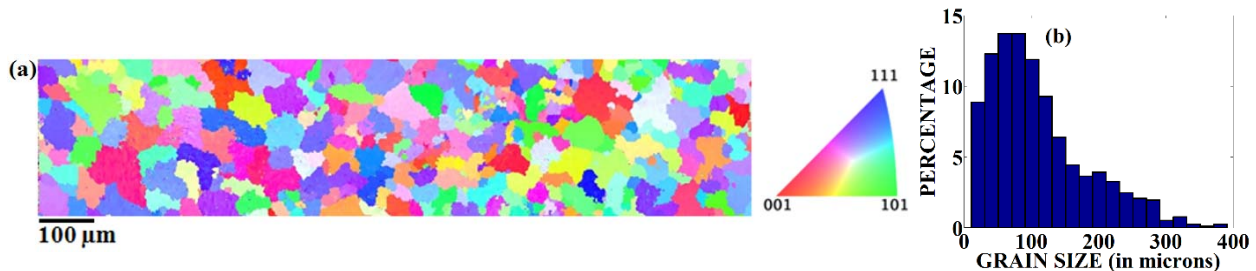

Fig. 2. a) EBSD scan of cast MAR-M247 taken in the polished section of the specimen and b) grain size distribution of cast MAR-M247.

Polished specimens were etched with Glyceregia (15 ml glycerol, 10 ml hydrochloric acid and 5 ml nitric acid) (Milenkovic et al. 2012; Rahimian et al. 2013), which helped reveal the microstructure of the material, when observed using an electron microscope. Following etching, images were obtained to study the composition and morphology of various types of carbide particles using energy dispersive spectroscopy (EDS) and secondary electron imaging, respectively. It was determined through EDS analysis that the carbide particles forming a continuous array along grain boundaries were rich in chromium (as shown in Fig. 3). The bulky carbide particles (like the particle shown in Fig. 3b) are comprised of Hafnium and Tantalum and are referred to as MC carbides. The coarser MC carbide particles, specifically with high aspect ratios, are highly brittle in nature and provide easy paths for rapid crack propagation thereby contributing to the degradation of ductility in the material (Kotval et al. 1972; Wawro 1982).
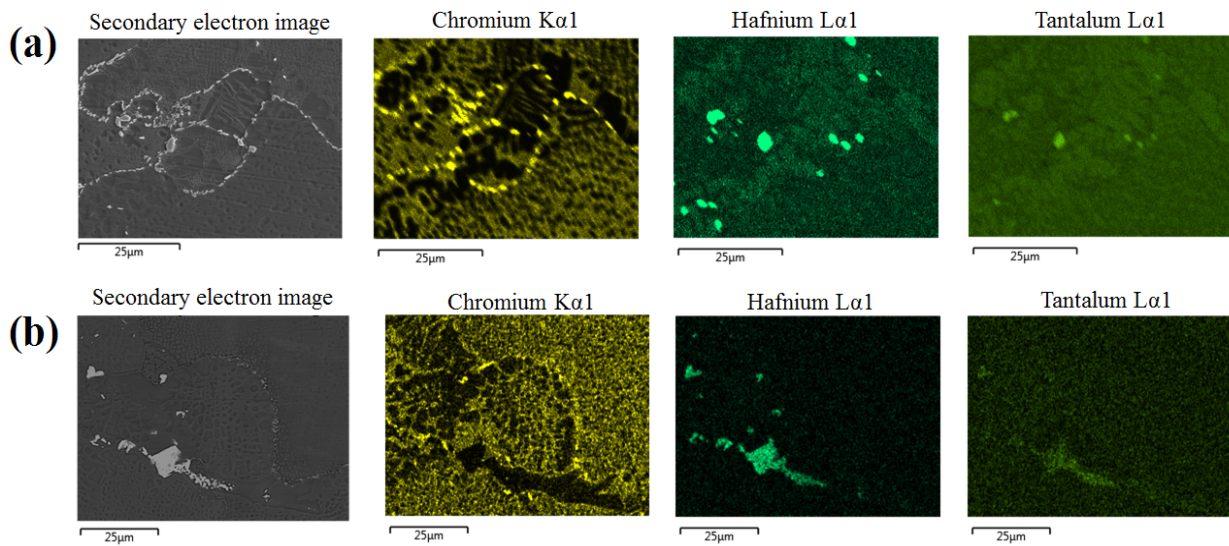

Fig. 3. (a) Secondary electron image and EDS analysis showing Chromium rich $M_{23}C_6$ particles which preferentially formed along grain boundaries. Also evident are a few scattered Hafnium and Tantalum rich particles that are larger than the Chromium rich $M_{23}C_6$ carbide particles. (b) Secondary electron image and EDS analysis of a bulky MC carbide particle shows that the particle has a high composition of Hafnium and Tantalum.

3. Fatigue test and DIC set-up

A double edge notch test specimen was subjected to displacement-controlled low-cycle fatigue testing at room temperature. Digital image correlation (DIC) technique was used to determine a peak displacement in such a way that the highest strain in the thinnest section of the specimen was 1.5%. Based on DIC strain measurements, a peak displacement value of 0.1825 mm, and a stress ratio (R) of 0.1 was used to prevent buckling of the specimens which were only 0.508 mm thick in the notch region. A 10% load drop was used as a fatigue test stop condition to observe cracks on the surface of the sample before failure. Once the fatigue test was stopped, the test specimen was analyzed using a scanning electron microscope to identify and study the crack initiation sites.

Stereo-microscopy together with DIC were used to record the imposed full-field strain on the thinnest region of the specimen. For this, the commercially available VIC-3D^{TM} system was

used at 2X magnification (using a 1.6X objective lens at a zoom level of 1.25), which resulted in a field of view of 8 x 7 mm² and a resolution of 3.34 μm per pixel. Two 5 mega-pixel cameras were used to capture the images at the peak load. DIC relies on tracking a visible surface pattern to measure displacement. In this study, an airbrush was used to deposit titanium oxide paint speckles, which ranged from 10 to 50 μm in diameter. This provided an acceptable resolution of 3 to 16 image pixels per pattern speckle. Further, the DIC parameters (including magnification, resolution, speckle dimensions, and field of view) were chosen with an intention of capturing macroscopic strain in the region of interest (thinnest section of the specimen), but not to obtain heterogeneous strains due to the complexities in the microstructure.

Because the images were obtained through a high-magnification lens, a distortion calibration procedure was necessary. Distortion was corrected in this case by taking 8 image pairs (left and right cameras) of a flat speckle pattern calibration target. The first image was taken at an arbitrary starting point on the calibration target. Subsequently, 4 images were taken along the horizontal axis, moving 15% of the image width each time, which then repeated for 4 additional images along the vertical axis. These images were then used to calibrate the distortion correction using the VIC-3D^{TM} software.

4. Results and discussion

4.1 Strain map from DIC

The strain map (in the loading direction) from the DIC technique obtained at peak displacement during the first fatigue cycle, at the thinnest section of the specimen is shown in Fig. 4. The maximum value of the strain component in the loading direction was calculated to be 1.5%. The specimen was cyclically loaded until a 10% load drop at peak displacement was observed. The specimen was then transferred to a scanning electron microscope for investigation of crack initiation sites.
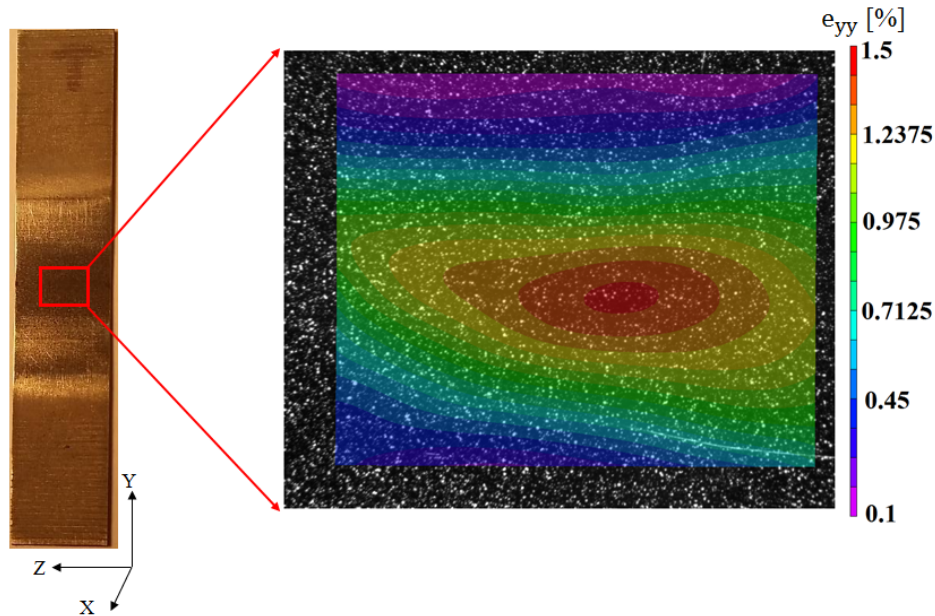

Fig. 4. Measurement of strain component in the loading direction (e_{yy}), in the thinnest section of a double edge notch specimen, using DIC technique. The loading axis is in the vertical direction. A speckle pattern was applied to the specimen.

4.2 Observations from electron microscopy

Through electron microscopy analysis, it was observed that several MC carbide particles cracked in the notch section of the specimen. Secondary electron images of 150 particles (80 uncracked and 70 cracked particles) were collected in order to analyze the area, aspect ratios of cracked carbide particles (calculated as the ratio between length of major and minor axis of a best fit ellipse), crack length within the cracked particles, and the angle made by the crack (within the cracked particle) with respect to the loading direction. All of the aforementioned metrics were collected using an open source image processing and analysis software, ImageJ (Schneider et al. 2012).

A correlation was found between particle cracking and the area of the particle on the surface of the specimen, which we refer to as surface area of particle. Figure 5 compares the area of cracked to uncracked carbide particles as cumulative probability. The average surface area of cracked carbide particles was approximately three times that of the average surface area of particles that were still intact, thereby showing that statistically, particles with larger surface area are more prone to crack incubation compared to smaller particles. This increased probability of crack incubation in particles with larger surface area can be attributed to many factors acting in concert, including but not limited to i) higher driving stress, ii) greater opportunity for larger carbide particles to interact with a higher number of slip bands impinging on them (compared to smaller particles), which results in the formation of more pileups at the intersection sites of the particles and slip bands, and iii) exposure to environmental effects (e.g. oxidation) increases with an increase in surface area, thereby promoting brittle fracture in particles with a large exposed surface area.
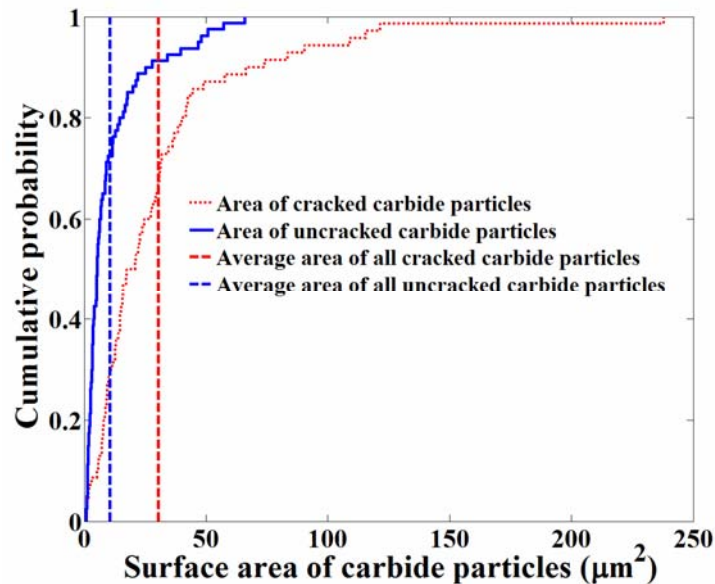

Fig. 5. Overlay of cumulative distributions of surface areas of cracked and uncracked carbide particles.

The angles made by several cracks (within the carbide particles) with the loading direction, θ, is plotted as a histogram in Fig. 6 and it is evident that most of the cracks aligned almost perpendicular to the loading direction. This is particularly true for most of the low aspect ratio

(aspect ratio less than 3) or equiaxed carbide particles. It is evident from Fig. 6 that the cracks in high aspect ratio particles are not perpendicular to the loading direction, and this is because they preferentially form along the largest dimension of the particle.
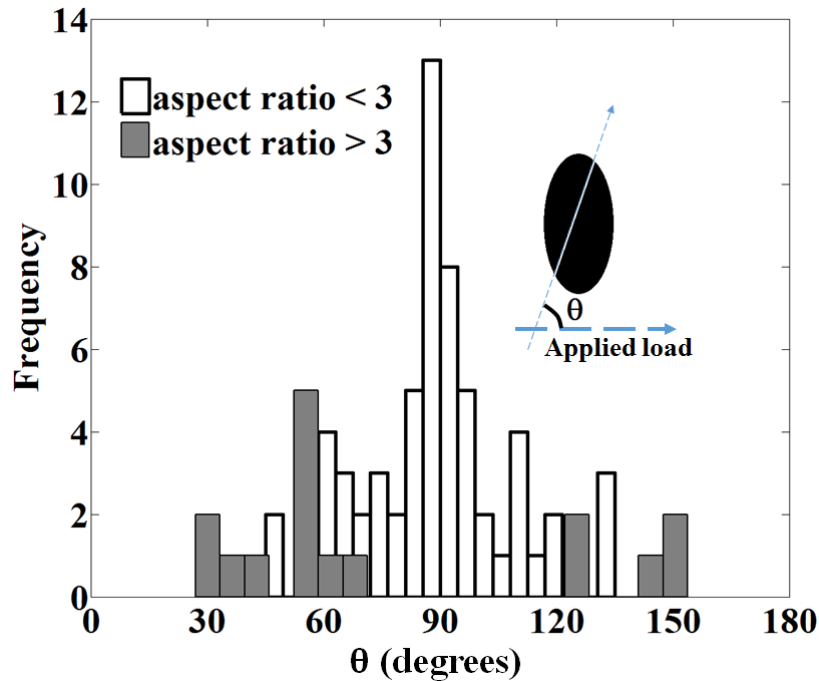

Fig. 6. Overlay of two histograms, with one showing the angles measuring the inclination of cracks (with the load direction) formed within 54 different carbide particles with aspect ratios less than 3, and the other histogram showing angles measuring the inclination of cracks (with the load direction) formed in carbide particles with aspect ratio greater than 3.

Additionally, forward-scattered imaging was used to capture the topographic contrast, which reveals information of slip bands in the local neighborhood of the cracked particles, which cannot be observed using secondary electron imaging. Forward-scattered electron images were taken in the vicinity of 40 particles (out of 150 particles whose size and shape metrics were evaluated from secondary electron images) to investigate the presence of slip bands. Slip bands impinging on the cracked carbide particles can be clearly observed in the forward-scattered images shown in Fig. 7. The interaction between the impinging slip bands and the brittle carbide particle causes dislocations to pile-up at the interaction sites, and thereby locally raising the stress and the internal strain energy within the carbide particle. The strain energy of the particle increases with cyclic loading until it reaches the fracture energy after which it results in the brittle fracture of the particle (Chang et al. 1979).
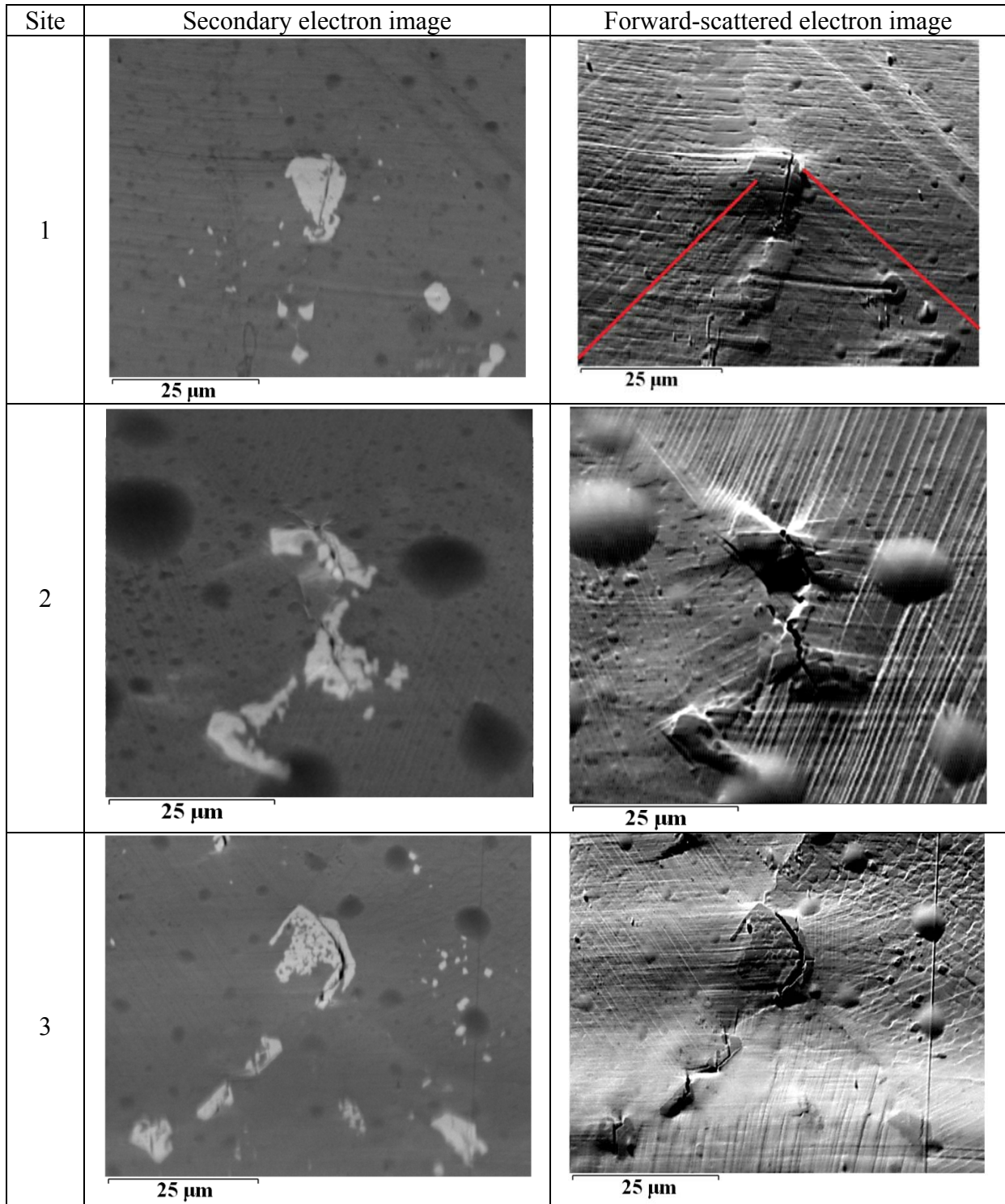
Site	Secondary electron image	Forward-scattered electron image
1		
2		
3		

Fig. 7. Secondary electron image and forward-scattered images of the neighborhoods of three cracked carbide particles. Forward-scattered images show the topology of the cracked carbide particles, γ-γ' matrix surrounding the particle and the impinging slip bands. In order to add further clarity regarding impinging slip bands, two slip band traces are displayed using red lines in site 1. The loading direction and specimen axis are horizontal for all images.

Impingement of slip bands was not observed at every particle in the highly strained region of the specimen. There were also cases where impingement of slip bands did not incubate cracks in particles, and some particles cracked without any sign of slip band impingement. Based on these observations, it can be inferred that although it is likely that the impingement of slip bands on carbide particles influences the propensity of crack incubation, it is not a necessary condition for particle cracking. Table 1 shows various scenarios observed with regards to slip band impingement and cracking. An observation from each of the cases in Table 1 (except for case including both slip band impingement and cracked particles, which are already shown in Fig. 7) are shown in Fig. 8. A few other factors that could play a potential role in driving particle crack incubation including residual stresses arising from the solidification process, misfit strains between the MC carbide particles and the γ-γ' matrix, and environmental effects (like oxidation) on carbide particles residing on the surface, have not been investigated in this current work.

Table 1. Data obtained regarding impingement of slip bands and particle cracking based on the investigation of forward-scattered images collected at 40 different particles in the highly strained region of the specimen

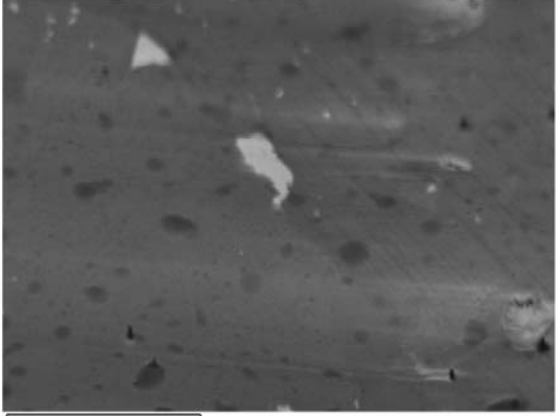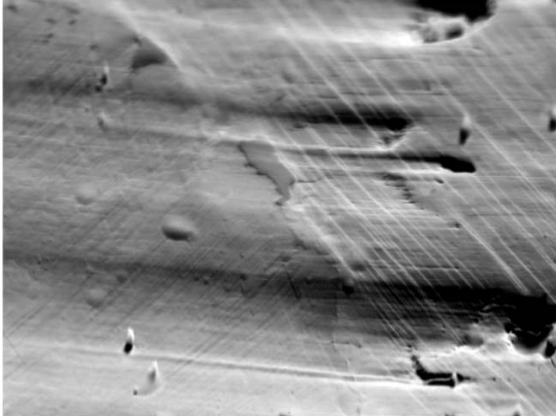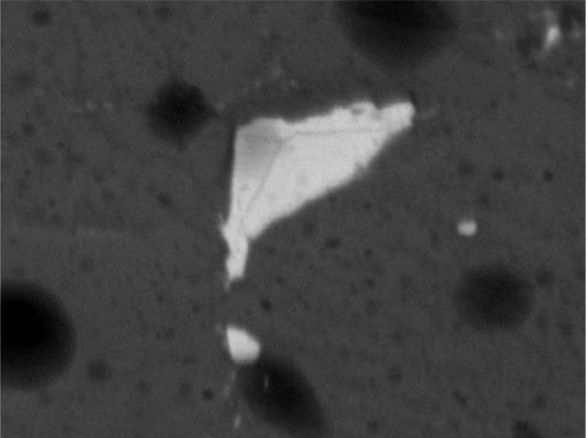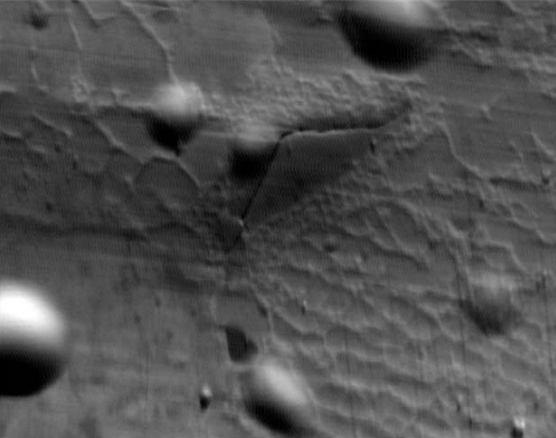| Slip band impingement	Number of cracked particles	Number of uncracked particles
Yes	29	3
No	4	4
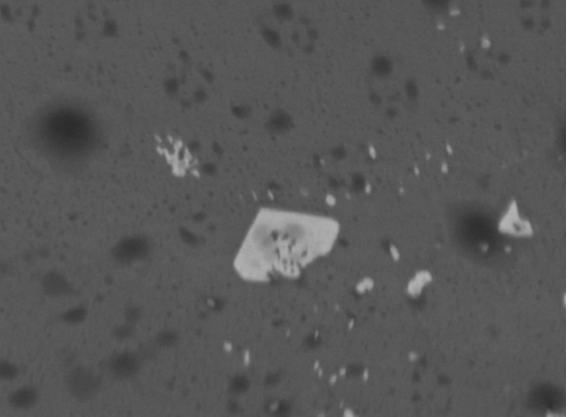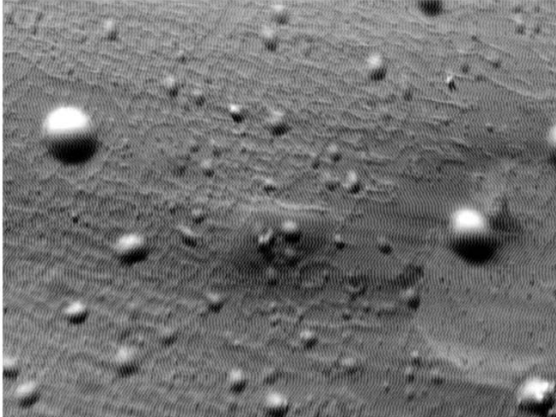
Site	Secondary electron image	Forward-scattered electron image
1		
2		
3		

Fig. 8. Secondary and forward-scattered electron images of 1) an intact carbide particle at a grain boundary being impinged by slip bands, 2) a cracked carbide particle with no trace of slip band impingement, and 3) an intact carbide particle with no trace of slip band impingement.

4.2.1 EBSD analysis in the neighborhood of cracked carbide particles

EBSD scans were taken in the vicinity of cracked carbide particles to study the surrounding matrix. It was evident from the EBSD maps (shown in Fig. 9) that many cracked carbides were located on grain boundaries. Localized elastic stresses arise due to significant differences in the elastic modulus of grains on either side of a grain boundary (Margolin 1998; Miao et al. 2009). In the current scenario, high localized stresses arise at the interface of the carbide particles with neighboring grains as there is i) lack of symmetry in crystal structure (between MC carbide particle and surrounding grains) and ii) significant difference in elastic moduli between anisotropic grains (whose elastic modulus ranges from 105 GPa to 280 GPa depending on their orientation (Stinville et al. 2016)) and carbide particles (which have an elastic modulus of 255 GPa (Li and Li 2010)). The impingement of slip bands, shown in Fig. 7, in combination with the high localized stresses developed within the particle act in concert to raise the strain energy of the carbide particle, and thereby increase the propensity of fracture of the particle (Chang et al. 1979).
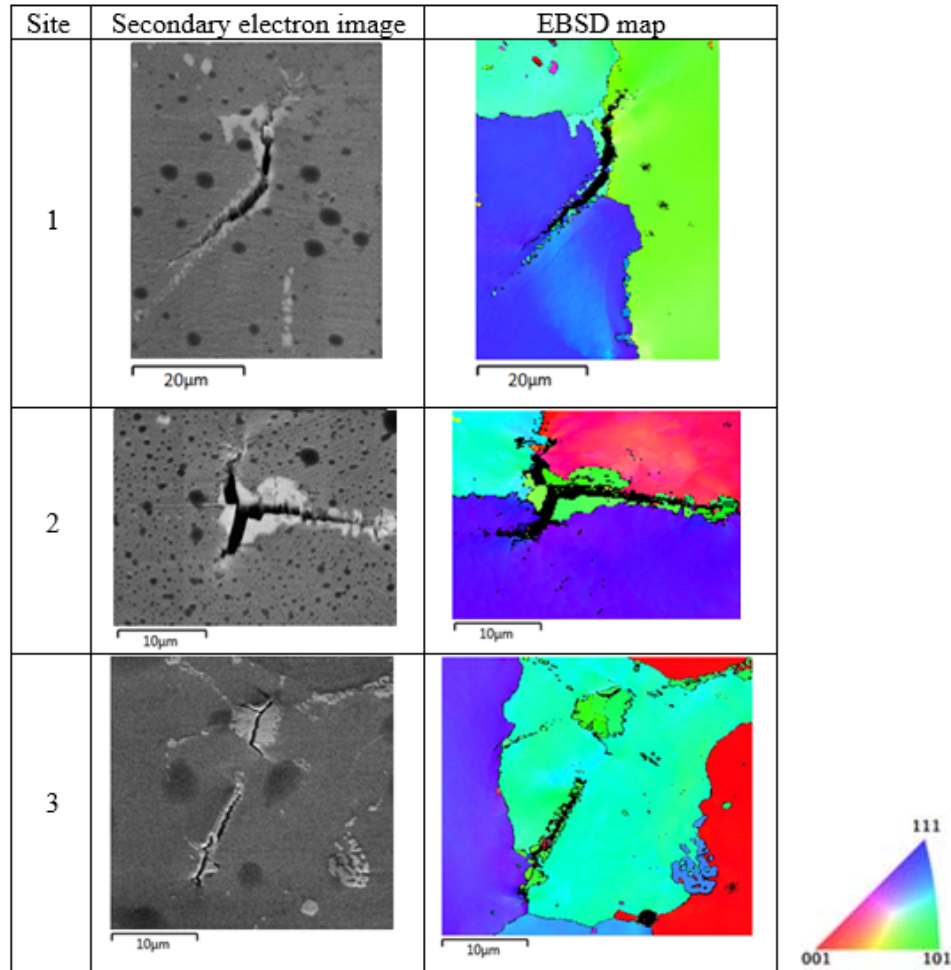

Fig. 9. Secondary electron images and EBSD maps of the local neighborhood of cracked carbides particles. Dark spots visible on the secondary electron image are the speckle pattern applied to the sample for DIC analysis. For all images, the loading axis and the specimen axis are in the horizontal direction.

4.3 Crystallographic crack growth in MAR-M247

Although cracks incubated from several carbide particles, only in a few cases did the incubated cracks within the carbides grow into the neighboring grains in a crystallographic fashion (as shown in Fig. 10). The crystallographic cracks, after being initiated from fractured carbides, coalesced together and grew into a large crack spanning over of coarse grains. One such crack was observed in the notch section of the specimen, which is located close to the region of highest strain in the DIC map (shown in Fig. 4), and grew perpendicular to the load direction (shown in Fig. 11). An EBSD analysis of the tip of this macroscopic crack shows that crystallographic cracking continues. To show how the crack growth lines up with localized deformation features, high resolution EBSD (HREBSD) post processing was performed (Ruggles et al. 2016). HREBSD analysis provides a map of geometrically necessary dislocation structure at the same length scale as the EBSD scan. Slip traces of the two slip planes involved in the cracking, the $(1\bar{1}1)$ and the $(11\bar{1})$, are shown on an HREBSD dislocation density map around the crack tip in Fig. 12. The dislocation density is not homogeneously distributed, but rather accumulates into geometrically necessary boundaries and slip bands with similar saturation values of dislocation density (around $2.5 \times 10^{14} m^{-2}$). From this dislocation density map (Fig. 12), it seems that plastic deformation ahead of the crack tip accumulates in the form of slip bands that facilitates crack growth. This apparent mechanism may be simulated to develop high fidelity crack growth models. Crystallographic crack growth even at a point when the crack has passed through several grains suggests that it is inadequate to use any crack growth model (for thin-walled specimens made of cast MAR-M247) that does not take into account the microstructure of the material.
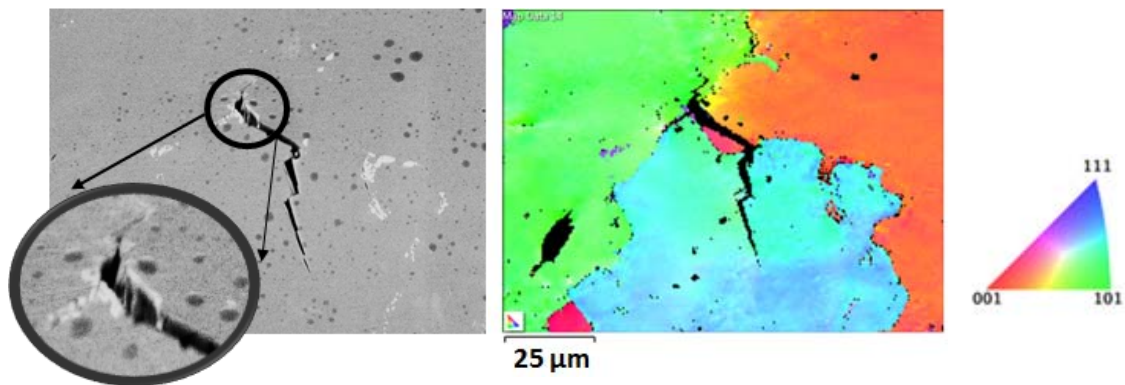

Fig. 10. Crystallographic crack growth observed for a fatigue crack that initiated within carbide. The location of the carbide is shown using a circle. The loading direction is horizontal.
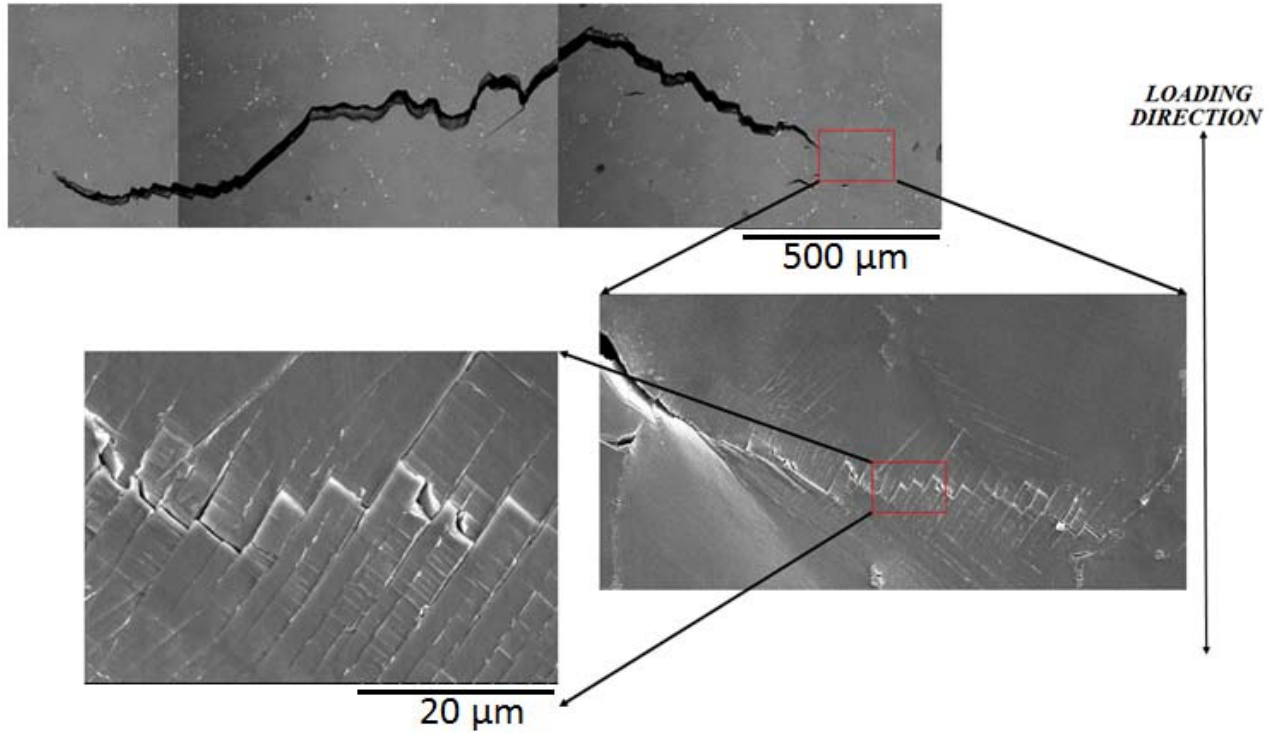
Fig. 11. Secondary electron image of a single large crack formed in the notch section of the specimen. Formation of surface extrusions and crystallographic crack growth can be seen in the enlarged images of a crack tip. The loading direction is vertical.

Fig. 12. Slip traces depicted on a dislocation density map of the region around the macroscopic crack tip for the a) $1\bar{1}1$ and b) $11\bar{1}$ slip systems. Note that the crack continues to grow crystallographically along slip bands of these two slip systems. The scale bar of dislocation density (in m/m^3) is shown in log scale. The cracks are shown in white. The loading direction is horizontal.

4.4 Crystal plasticity analysis to statistically study the stress state of carbide particles

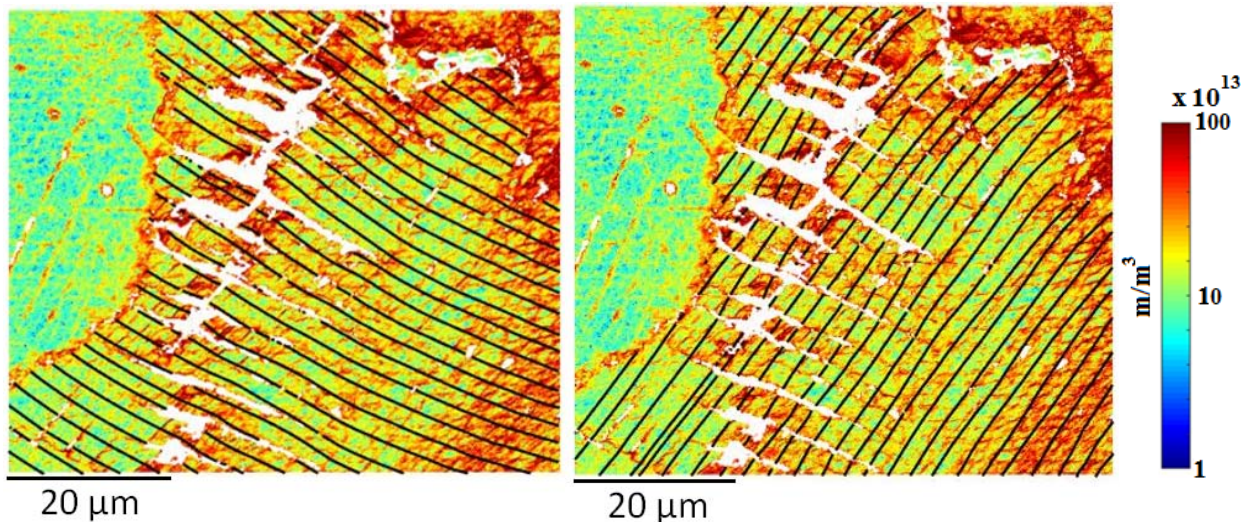It was evident from microscopy observations that not all the carbide particles (present on the surface of the notch section of the specimens) cracked, for example sites 1 and 3 shown in Fig. 8. It was of interest to understand the fundamental reasons why some particles are more vulnerable to crack incubation than other particles. Although microscopic imaging coupled with EBSD provides valuable information regarding the deformation mechanisms leading to crack incubation and initiation, it does not provide information regarding the complex 3D stress state of the particles, and the surrounding grains, which appears to be a governing variable driving crack incubation. In order to study the complex stress state in particles, it is necessary to take into consideration the heterogeneous microstructure surrounding the carbides, and capture the influence of the neighboring grains on the stress state of carbide particles.

For this purpose, a CPFE framework was used to statistically study the stress state of the carbide particles. Synthetic microstructures were created based on the statistics of the microstructures: grain morphology obtained from EBSD and particles' sizes and aspect ratios from X-Ray CT data. The aforementioned statistical attributes of cast MAR-M247 were used to create several instantiations of the microstructure of MAR-M247, using DREAM.3D (Groeber and Jackson 2014). For the purpose of this study, synthetic microstructures were created considering only the Hafnium and Tantalum rich MC particles present at grain boundaries, and ignoring the Chromium-rich $M_{23}C_6$ particles, due to the high frequency of cracking at MC particles. Further, the γ -γ' phase was homogenized, by not explicitly introducing the γ' particles. Surface meshes of all the grains comprising the microstructure were input into Gmesh (Geuzaine and Remacle 2009) which generated a tetrahedral volume mesh of the microstructure. This volume mesh was then input into an in-house finite element code, ScIFEi (Warner et al. 2016), to carry out the computationally-intensive simulations to solve for the heterogeneous stress and strain state within the microstructure.

4.4.1 Crystal plasticity framework

A CPFE framework was used to solve for the heterogeneous stress state within the polycrystalline microstructure by combining anisotropic elasticity with rate dependent crystal plasticity kinetics. For the elastic behavior, individual grains representing the γ -γ' matrix were assigned cubic elastic constants C_{11}, C_{12} and C_{44} equal to 258.6 GPa, 167.0 GPa, 125.0 GPa respectively (Brindley et al. 2015), while the MC carbide particles were assigned isotropic elastic properties, Young's modulus and Poisson's ratio equal to 255 GPa and 0.33, respectively (Li and Li 2010). No plasticity model was applied to the carbide particles, as it is well known that these particles are brittle. Rate-dependent crystal plasticity kinetics (flow rule and hardening law) were assigned for the γ -γ' matrix. Since the experiments were conducted at room temperature, it has been assumed that the plastic flow occurs only through dislocation glide on cubic slip systems within the γ -γ' matrix, while octahedral slip is not activated. The flow rule used for describing incremental slip on the cubic slip systems is shown in Eq. 1

$$\dot{\gamma}^\alpha = \dot{\gamma}_0 \frac{\tau^\alpha}{g^\alpha} \left| \frac{\tau^\alpha}{g^\alpha} \right|^{\frac{1}{m}-1} , \qquad (1)$$

where $\dot{\gamma}^\alpha$ and $\dot{\gamma}_o$ are the shear and reference shear rates of slip system α, respectively, m is a shear rate sensitivity parameter, τ^α is the resolved shear stress acting on a slip system α, and g^α is critical resolved shear stress representing the delay in the onset of plastic deformation.

The slip resistance ($\dot{g}^\alpha$) shown in Eq. 2 evolves according to a gradient based evolution law obtained from combining the hardening laws given by Beaudoin et al. (Beaudoin et al. 2000) and Voce-Kocks relations (Kocks 1976)

$$\dot{g}^\alpha = H_o \frac{\beta^2 \mu^2 b}{2(g^\alpha - g_o^\alpha)} \sum_{k=1}^{N_{SS}} \sqrt{(\hat{n}_p^k : \Delta^T)(\Delta : \hat{n}_p^k)} |\dot{\gamma}^k| + G_o \left(\frac{g_s^\alpha - g^\alpha}{g_s^\alpha - g_o^\alpha}\right) \sum_{k=1}^{N_{SS}} |\dot{\gamma}^k| , \qquad (2)$$

where g_o^α and g_s^α are the initial and saturation resolved shear strengths of slip system α, N_{SS} represents the number of slip systems, H_o and G_o are the direct hardening coefficients, $\beta=\frac{1}{3}$ (Cerrone et al. 2015), b is the Burgers vector, $\hat{n}_p$ is the slip plane normal, μ an elastic constant equal to C_{44}, Δ is the measure of dislocation density and is calculated using the gradient of plastic deformation as shown in Eq. 3,

$$\Delta_{ij} = \epsilon_{jkl} F_{il,k}^p . \qquad (3)$$

There are a total of 6 calibration parameters ($\dot{\gamma}_o$, m, H_o, G_o, g_o^α and g_s^α) in the crystal plasticity model used in the current framework. The parameters were iteratively tuned in order to fit the macroscopic stress strain curve of MAR-M247 at room temperature, obtained from Liao et al. (Liao et al. 2010). The final calibration parameters of the crystal plasticity framework are shown in Table 2.

Table 2. Calibrated parameters to fit the macroscopic stress strain curve of MAR-M247 at room temperature.

Parameter	Value
$\dot{\gamma}_o$ (s^{-1})	0.98
m	0.045
H_o (MPa)	412.3
G_o (MPa)	415.2
g_o^α (MPa)	320.2
g_s^α (MPa)	375.2

4.4.2 Polycrystal simulations

Three statistically representative polycrystal models of the MAR-M247 microstructure were generated to study the variation of particle stress state due to variation in neighboring microstructure. One of the microstructure models created using the workflow described in Section 4.3 is shown in Fig. 13. A strain of 1.5% was applied to the synthetic microstructures using displacement controlled loading, and the stress state of the carbide particles was collected at maximum displacement. The boundary conditions applied on the microstructure model are described in Table 3. Maximum principal stress was calculated at every material point in all the

15

carbide particles (which were assigned a linear elastic material). In order to study the variation of stress state among all the carbide particles, maximum principal stress values obtained at all the material points in all carbide particles in the microstructure were pooled together to create a cumulative distribution, shown in Fig. 14. This was overlaid with the cumulative distributions of the principal stresses in two carbide particles (with minimum and maximum values of the volumetric average principal stress values).
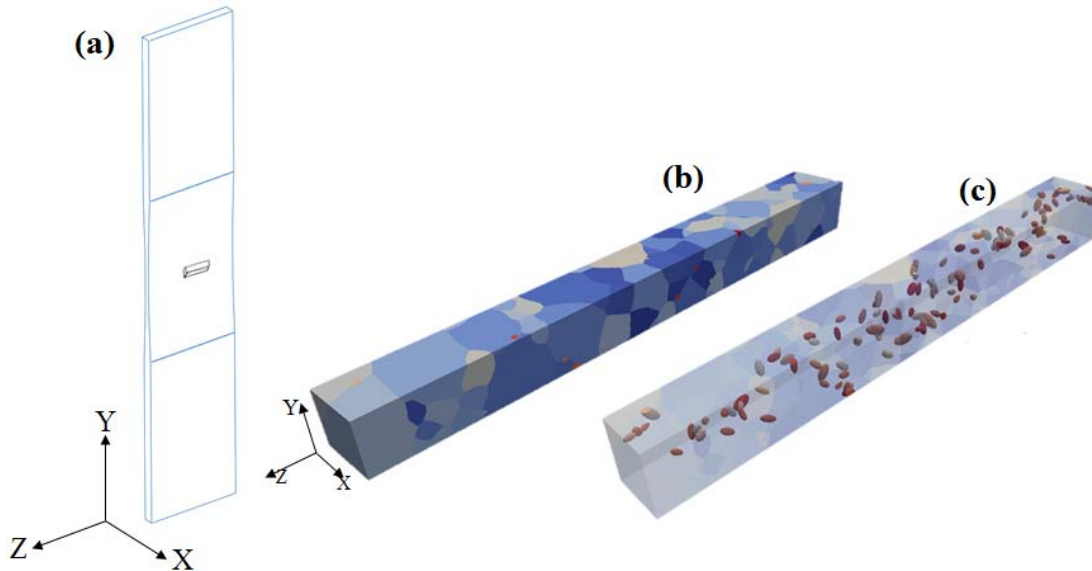

Fig. 13. (a) 3D rendering of the specimen showing the coordinate axis and the location at which the microstructure volume is being modeled (b) A statistically representative polycrystal model of MAR-M247, with MC carbide particles at the grain boundaries. This particular microstructure has 235 features (120 grains and 115 carbide particles) in a volume of 200x200x2000 μm, with a resolution of 2 μm per voxel. (c) Opacity of the same microstructure was adjusted to distinctly show all the carbide particles inserted at grain boundaries.

Table 3. Model boundary conditions.

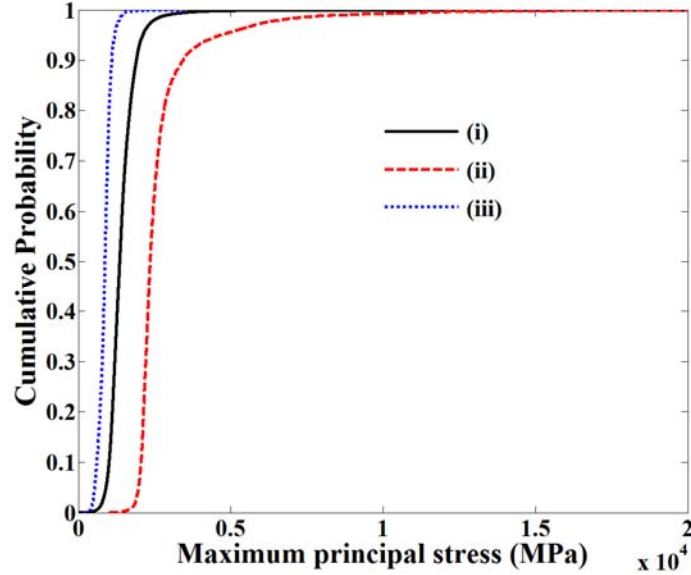| Boundary face	Boundary condition
-X	Fix X displacement
+X	Free
-Y	Fix Y displacement
+Y	Apply Y displacement
-Z	Fix Z displacement
+Z	Free

Fig. 14. Cumulative probability distribution plot showing the variation in the maximum principal stress in carbide particles. The black curve (i) represents the principal stress collected at every integration point in all carbide particles throughout the microstructure. The red curve (ii) corresponds to distribution of maximum principal stress in a carbide particle which has the highest value of the volumetric average of maximum principal stress, and the blue curve (iii) corresponds to distribution of maximum principal stress in a carbide particle which has the lowest value of the volumetric average of maximum principal stress. The maximum principal stress state of particles was computed at 1.5% applied strain.

Although all carbide particles were assigned the same isotropic linear elastic material property, there is a significant variation in the stress state of the particles. To understand the driving forces for crack incubation in the particles, and to answer the fundamental question of why only some particles crack and some do not (as observed through microscopy scans in highly strained region in the specimen), it is important to investigate the factors responsible for a significant variation of stress state of the particles. For this purpose, two different factors were considered in this study i) influence of the stress state of the grains surrounding the carbide particles and ii) influence of location of the particle on the surface or within the bulk of the microstructure.

First, to study the influence of the stress state of the neighboring microstructure on the stress state of a carbide particle, an average stress component (σ_{yy}, with yy being in the loading direction) was computed for all the particles, and their corresponding neighbors. Average stress state in a complex deformation domain is not representative of the overall heterogeneous volumetric stress state of the carbide particle, but this metric was chosen to estimate a first order influence of the stress state of the neighboring microstructure surrounding the carbide particle. From three unique synthetic microstructures, the average stress state of 334 carbide particles, and the stress states of their immediate neighboring grains was collected, and the corresponding plot obtained from the data is shown in Fig.15. Each data point in Fig.15 corresponds to the average stress state of the carbide particle and the volume occupied by the grains surrounding a particle. There is an overall positive correlation between the average stress state of the neighboring grains and the average stress state of the carbide particles. In addition to the correlation, there is also a

17

significant variation in the stress state of the carbide, for a given average stress state of the carbide neighborhood volume, occupied by its neighboring grains.
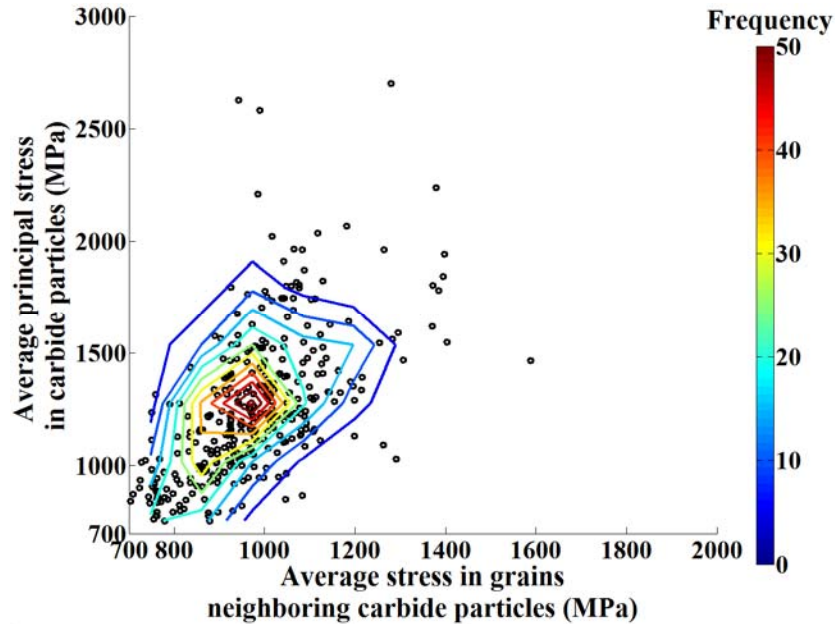

Fig. 15. Scatter plot overlaid on a density contour plot to show a correlation between the average stress component (in loading direction, σ_{yy}) in carbide particles and corresponding average stress component in the grains neighboring each carbide particle. Values on the color bar represents frequency, which is equivalent to the height of the 3D surface plot constructed from a bivariate histogram created on a rectangular grid, using the scatter data.

In addition to the orientation of grains, it was of interest to investigate the stress experienced by particles based on their location either contained within the bulk of the material or intersecting the surface. For this purpose, the stress state of the particles which reside in the bulk of the microstructure were compared to those on the surface. First, the major principal stress was computed at every integration point in the particles. The average value of the major principal stress was calculated by taking the average of the major principal stresses calculated at all the integration points throughout the carbide particle. Similarly, the maximum values of the major principal stresses were calculated for every particle. By pooling together the two aforementioned metrics (average and maximum values of major principal stress) for all the particles in a microstructure, cumulative distributions of the metrics were created. Separate distributions were created for particles that are on the surface and for those that reside within the bulk of the microstructure. The distributions were overlaid as shown in Fig. 16. From the cumulative distribution plots, it is clear that the carbide particles on the surface are subject to higher stresses than those that are within the bulk of the microstructure. The carbide particles within the bulk of the microstructure are completely surrounded by grains, which, based on their crystallographic orientation, constrain the deformation of the particle and control the load (and hence stress) acting on the particle. For the particles that are on the surface, there is less constrained volume, as it is exposed to the free surface. Consequently, the carbide particles on the surface are subject to statistically higher deformations, which lead to higher stresses. Apart from the stress based effects, there are also environmental

effects (not considered in the simulations done in this study) which may make the carbide particles more vulnerable to brittle fracture, compared to those which reside within the bulk of the material.
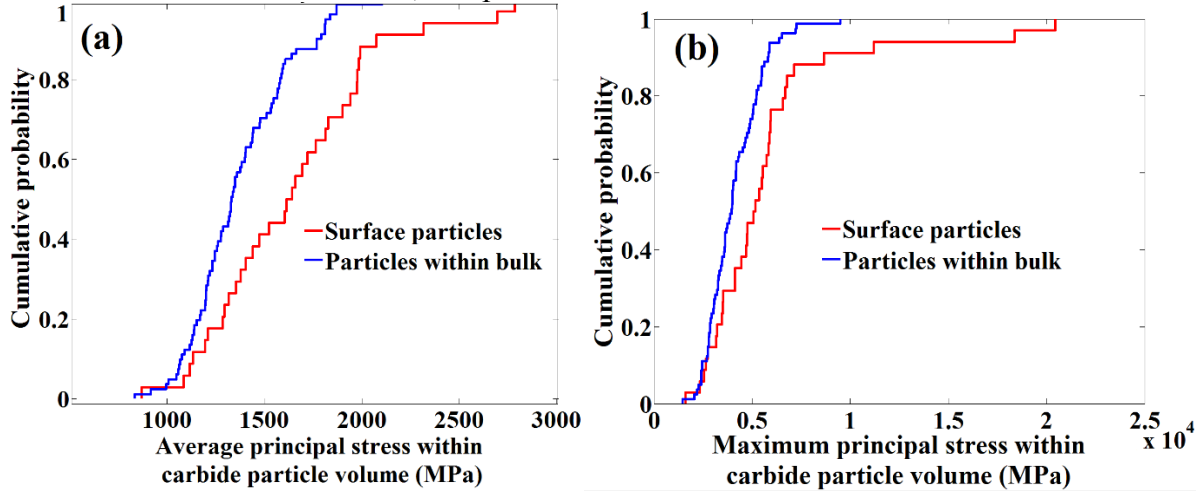

Fig. 16. (a) Cumulative distribution plots obtained by pooling together the volumetric average principal stress values of all surface and bulk carbide particles at 1.5% applied strain, (b) Cumulative distribution plots obtained by pooling together the volumetric maximum principal stress values of all surface and bulk carbide particles at 1.5% applied strain.

For each particle within the microstructure, the angle (θ') made by the normal to the major principal stress axis with the loading direction was calculated with an interest to study if there existed any correlation between θ' and θ, which is the angle made by the cracks formed within carbide particles with respect to loading direction (as shown in Fig. 6). For this purpose, an average stress tensor was calculated, by averaging the stress tensor derived at every element within the volume of a carbide particle. The major principal stress axis for the average stress tensor of each carbide particle was calculated and the angle made by the normal of the major principal stress axis was calculated with respect to the applied load direction. Thus, each carbide particle is associated with an average stress tensor, a principal stress axis, and the orientation the principal stress axis and its normal makes with the applied load. The aforementioned data was obtained for 334 carbide particles (present in the three virtual microstructures created for this study), which were segregated into two sets based on their aspect ratios. The first set consisted of 252 particles with each particle having both the aspect ratios, $\frac{a}{b}$ and $\frac{a}{c}$ (with a being length of the major axis, b and c being lengths of the minor axes) being less than 3, and the second set consisted of 82 particles which have at least one of the two aspect ratios greater than 3. θ' was calculated for particles in both sets of particles and the data was plotted as an overlay of histograms, as shown in Fig. 17. It is evident from Fig. 17 that the normal to the major principal axis is aligned mostly perpendicular to the loading direction, which also implies that the major principal stress axis is closely aligned with the applied load direction. This close alignment of the principal stress axis with the applied load could significantly influence the formation of cracks perpendicularly to the applied load axis, as observed in experiments (Fig. 6).

However, the results shown in Fig. 17 do not explain why the cracks formed within the carbide particles with aspect ratios greater than 3 are frequently not perpendicular to the applied load direction (as shown in Fig. 6). In order to explain why cracks form along the major axis of

19

high aspect ratio carbide particles, more realistic modeling would be required. For instance, assigning orientations to the MC carbide particles would be necessary, as these particles exhibit crystallographic heterogeneity. Additionally, appropriate anisotropic elastic moduli need to be calculated for the MC carbide particles (from molecular dynamic or density functional theory simulations) and those properties need to be used to study how the stress state of the particle would change depending on orientation between the particle and the surrounding grains. The aforementioned studies based on the anisotropy of the MC particles to address why cracks are aligned along the major axis of high aspect ratio MC particles are beyond the scope of the current work.
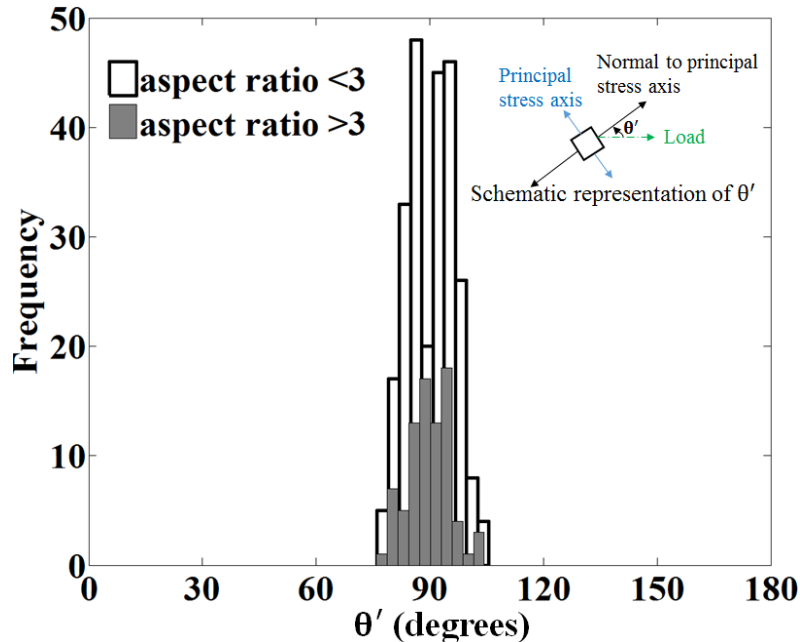

Fig. 17. Plot showing the angle (θ') made by the normal to major principal stress axis with the loading direction, in two sets of carbide particles, collected from three virtual microstructures which were subject to a strain of 1.5%.

CPFE simulation results using virtual microstructures of MAR-M247 statistically show the significant influence of the crystallographic orientation of neighboring grains and location of carbide particles (surface vs. bulk) on the stress state of the carbide particles. The CPFE framework used in the current work does not take into consideration i) the interaction between brittle particles and slip bands, ii) the misfit strains between the MC carbide particles and the γ- γ' matrix, iii) the residual stresses and strains arising from the casting process, and iv) environmental effects on the carbide particles present on the surface of the component all of which play a collective role in the brittle fracture of particles.

5. Conclusions

The following conclusions are drawn from this work:

• Fatigue cracks incubated extensively at large Hafnium/Tantalum rich MC carbide particles on the grain boundaries, when MAR-M247 was subject to low cycle fatigue at room temperature.

• Analysis of secondary electron images showed that the surface area of cracked particles was approximately three times that of the uncracked particles. Further, it was determined that the cracks aligned nearly perpendicular to the loading direction in particles with aspect ratios less than 3, the cracks predominantly aligned with the major axis, in particles with high aspect ratios.

• Through forward-scattered electron imaging, it was observed that a significant number of slip bands interacted with a large number of carbide particles which cracked. Fewer particles were still intact upon the impingement of slip bands. Although impingement of slip bands drives the propensity of crack incubation in particles, it is not a sufficient condition (or single most influential criterion) to incubate a crack.

• Microscopy analysis showed that a large life-limiting crack grew crystallographically, even when spanning the length of multiple grains. HREBSD analysis showed that the crack grew along slip bands of two active slip systems.

• Crystal plasticity finite element (CPFE) simulations that were run using virtual microstructures of MAR-M247 showed a significant variability in the stress state among several carbide particles and that it is governed by the stress state of the neighboring grains. Further, it was observed from simulations that the particles on the surface experience higher stresses compared to particles within the bulk of the material.

• CPFE simulations show that the normal to the major principal stress axis (calculated in hundreds of carbide particles) aligned predominantly perpendicular with the loading direction, irrespective of the aspect ratio of the particles.

Acknowledgements

References

Beaudoin AJ, Acharya A, Chen SR, et al. (2000) Consideration of grain-size effect and kinetics in the plastic deformation of metal polycrystals. Acta Mater 48:3409–3423. doi: 10.1016/S1359-6454(00)00136-1

Boismier DA, Sehitoglu H (1990) Thermo-Mechanical Fatigue of Mar-M247: Part 1— Experiments. J Eng Mater Technol Trans ASME 112:68. doi: 10.1115/1.2903189

Bor HY, Chao CG, Ma CY (1999) The effects of Mg microaddition on the mechanical behavior and fracture mechanism of Mar-M247 superalloy at elevated temperatures. Metall Mater Trans A 30:551–561. doi: 10.1007/s11661-999-0047-3

Bowman R, Ritzert F, Freedman M (2004) Evaluation of Candidate Materials for a High-Temperature Stirling Convertor Heater Head. In: Space Technology and Applications International Forum. Melville, NY, pp 821–828.

Bozek JE, Hochhalter JD, Veilleux MG, et al. (2008) A geometric approach to modeling microstructurally small fatigue crack formation: I. Probabilistic simulation of constituent particle cracking in AA 7075-T651. Model Simul Mater Sci Eng 16:65007. doi: 10.1088/0965-0393/16/6/065007

Brindley KA, Kirka MM, Fernandez-Zelaia P, Neu RW (2015) Thermomechanical fatigue of Mar-M247: Extension of a unified constitutive and life model to higher temperatures. J Eng Mater Technol Trans ASME. doi: 10.1115/1.4029908

Cerrone A, Stein C, Pokharel R, et al. (2015) Implementation and verification of a microstructure-based capability for modeling microcrack nucleation in LSHR at room temperature. Model Simul Mater Sci Eng 23:35006. doi: 10.1088/0965-0393/23/3/035006

Chang R, Morris WL, Buck O (1979) Fatigue crack nucleation at intermetallic particles in alloys — A dislocation pile-up model. Scr Metall 13:191–194. doi: 10.1016/0036-9748(79)90291-6

Chen J, Lee J, Jo C, et al. (1998) MC carbide formation in directionally solidified MAR-M247 LC superalloy. Mater Sci Eng A 247:113–125. doi: 10.1016/S0921-5093(97)00761-2

Gell M, Leveran GR (1968) The Fatigue of the nickel-Base superalloy Mar-M200 in single crystal and columnar-grained forms at room temperature. Trans TMS-AIME 242:1869–1879.

Geuzaine C, Remacle JF (2009) Gmsh: A 3-D finite element mesh generator with built-in pre- and post-processing facilities. Int J Numer Methods Eng 79:1309–1331. doi: 10.1002/nme.2579

Groeber M, Jackson M (2014) DREAM.3D: A Digital Representation Environment for the Analysis of Microstructure in 3D. Integr Mater Manuf Innov 3:5. doi: 10.1186/2193-9772-3-5

Janowski GM (1985) The effect of Tantalum on the structure/properties of two polycrystalline nickel-base superalloys: B-1900+Hf and MAR-M247, NASA Contractor Report 174847.

Kaufman M (1984) Properties of Cast Mar-M-247 for Turbine Blisk Applications. In: Superalloys 1984 (Fifth International Symposium). TMS, pp 43–52.

Kocks F (1976) Laws for Work-Hardening and Low-Temperature creep. J Eng Mater Technol 98:76–85. doi: 10.1115/1.3443340

Kotval PS, Venables JD, Calder RW (1972) The role of hafnium in modifying the microstructure of cast nickel-base superalloys. Metall Trans 3:457–462. doi: 10.1007/BF02642049

Li G, Li G (2010) Microstructure and mechanical properties of hafnium carbide coatings synthesized by reactive magnetron sputtering. J Coatings Technol Res 7:403–407. doi: 10.1007/s11998-009-9225-x

Liao J-H, Bor H-Y, Chao C-G, Liu T-F (2010) Effects of Rhenium on Microstructure and Phase Stability of MAR-M247 Ni-Base Fine-Grain Superalloy. Mater Trans 51:810–817. doi: 10.2320/matertrans.M2009331

Margolin H (1998) Polycrystalline yielding—perspectives on its onset. Acta Mater 46:6305–6309. doi: 10.1016/S1359-6454(98)00227-4

Miao J, Pollock TM, Wayne Jones J (2009) Crystallographic fatigue crack initiation in nickel-based superalloy René 88DT at elevated temperature. Acta Mater 57:5964–5974. doi: 10.1016/j.actamat.2009.08.022

Milenkovic S, Sabirov I, Llorca J (2012) Effect of the cooling rate on microstructure and hardness of MAR-M247 Ni-based superalloy. Mater Lett 73:216–219. doi: 10.1016/j.matlet.2012.01.028

Nathal MV, Maier RD, Ebert LJ (1982) The influence of cobalt on the tensile and stress-rupture properties of the nickel-base superalloy MAR-M247. Metall Trans A 13:1767–1774. doi: 10.1007/BF02647832

Przybyla C, Prasannavenkatesan R, Salajegheh N, McDowell DL (2010) Microstructure-sensitive modeling of high cycle fatigue. Int J Fatigue 32:512–525. doi: 10.1016/j.ijfatigue.2009.03.021

Rahimian M, Milenkovic S, Sabirov I (2013) Microstructure and hardness evolution in MAR-

M247 Ni-based superalloy processed by controlled cooling and double heat treatment. J Alloys Compd 550:339–344. doi: 10.1016/j.jallcom.2012.10.129

Ruggles TJ, Fullwood DT, Kysar JW (2016) Resolving geometrically necessary dislocation density onto individual dislocation types using EBSD-based continuum dislocation microscopy. Int J Plast 76:231–243. doi: 10.1016/j.ijplas.2015.08.005

Schneider CA, Rasband WS, Eliceiri KW (2012) NIH Image to ImageJ: 25 years of image analysis. Nat Methods 9:671–675. doi: 10.1038/nmeth.2089

Schreiber JG, Thieme LG (2008) GRC supporting technology for NASA's Advanced Stirling Radioisotope Generator (ASRG). AIP Conf Proc 969:582–592. doi: 10.1063/1.2845018

Sehitoglu H, Boismier DA (1990) Thermo-Mechanical Fatigue of Mar-M247: Part 2—Life Prediction. J Eng Mater Technol 112:80. doi: 10.1115/1.2903191

Shenoy MM, Kumar RS, McDowell DL (2005) Modeling effects of nonmetallic inclusions on LCF in DS nickel-base superalloys. Int J Fatigue 27:113–127. doi: 10.1016/j.ijfatigue.2004.06.008

Šmíd M, Horník V, Hutař P, et al. (2016) High Cycle Fatigue Damage Mechanisms of MAR-M 247 Superalloy at High Temperatures. Trans Indian Inst Met 69:393–397. doi: 10.1007/s12666-015-0817-0

Šmíd M, Kunz L, Hutař P, Hrbáček K (2014) High cycle fatigue of nickel-based superalloy MAR-M 247 at high temperatures. Procedia Eng 74:329–332. doi: 10.1016/j.proeng.2014.06.273

Stinville JC, Lenthe WC, Miao J, Pollock TM (2016) A combined grain scale elastic-plastic criterion for identification of fatigue crack initiation sites in a twin containing polycrystalline nickel-base superalloy. Acta Mater 103:461–473. doi: 10.1016/j.actamat.2015.09.050

Szczotok A, Rodak K (2012) Microstructural studies of carbides in MAR-M247 nickel-based superalloy. IOP Conf Ser Mater Sci Eng 35:12006. doi: 10.1088/1757-899X/35/1/012006

Szczotok A, Szala J, Cwajna J, Hetmańczyk M (2006) Selection of etching methods of primary carbides in MAR-M247 nickel-base superalloy for computer-aided quantitative metallography. Mater Charact 56:348–354. doi: 10.1016/j.matchar.2005.10.011

Warner JE, Bomarito GF, Hochhalter JD (2016) Scalable Implementation of Finite Elements by NASA _ Implicit (ScIFEi), NASA/TM - 2016-219180, Hampton, Virginia.

Wawro SW (1982) MC carbide structures in Mar-M247, NASA Contractor Report 167892.

Wood JG, Carroll C, Matejczyk D, Penswick L (2005) Advanced 80 W_e stirling convertor phase II development progress. 3rd Int Energy Convers Eng Conf. doi: 10.2514/6.2005-5559

Zhang J, Prasannavenkatesan R, Shenoy MM, McDowell DL (2009) Modeling fatigue crack nucleation at primary inclusions in carburized and shot-peened martensitic steel. Eng Fract Mech 76:315–334. doi: 10.1016/j.engfracmech.2008.10.011